Rapid Communications

Time–Frequency MEG-MUSIC Algorithm

Kensuke Sekihara,* Srikantan Nagarajan,
David Poeppel, and Yasushi Miyashita

***Abstract*—We propose a method that incorporates the time–frequency characteristics of neural sources into magnetoencephalographic (MEG) source estimation. The method is based on the multiple-signal-classification (MUSIC) algorithm and it calculates a time–frequency matrix in which diagonal and off-diagonal terms are the auto and crosstime–frequency distributions of multichannel MEG recordings, respectively. The method averages this time–frequency matrix over the time–frequency region of interest. The locations of neural sources are then estimated by checking the orthogonality between the noise subspace of this averaged matrix and the sensor lead field. Accordingly, the method allows us to estimate the locations of neural sources from each time–frequency component. A computer simulation was performed to test the validity of the proposed method, and the results demonstrate its effectiveness.**

***Index Terms*— Biomagnetism, biomedical signal processing, inverse problems, time–frequency analysis.**

I. Introduction

THE noninvasive measurement of magnetic fields generated from human cortical neural activities, referred to as magnetoencephalography (MEG) [1], has been found to be a powerful tool in studies of human neurophysiology and neural information processing. One major problem here is the MEG inverse problem [1], a problem of estimating neural current distributions from the magnetic field measured outside a human head. Because the neural current distribution is inherently three-dimensional (3-D), the estimation problem is generally ill posed. To reduce this ill posedness, the estimation needs to incorporate some prior knowledge regarding the source characteristics. Such characteristics can include possible source locations, the source spatial extent, the total number of sources, or the source-frequency characteristics. In this paper, we propose a novel method that incorporates source time–frequency characteristics into the source estimation. The method combines time–frequency analysis [2] with the MEG multiple-signal-classification (MUSIC) algorithm [3] and allows estimation of neural sources from each time–frequency component. Throughout this paper, plain italics indicate scalars, lower case boldface italics indicate vectors, and upper case boldface italics indicate matrices. The superscript T indicates the matrix transpose and $\boldsymbol{I}$ indicates the unit matrix. The eigenvalues are numbered in decreasing order.

Manuscript received July 15, 1998; revised December 7, 1998. This work was supported in part by the Centre National de la Recherche Scientifique. The Associate Editor responsible for coordinating the review of this paper and recommending its publication was M. Viergever. *Asterisk indicates corresponding author.*

*K. Sekihara is with the Mind Articulation Project, Japan Science and Technology Corporation (JST), Yushima 4-9-2, Bunkyo, Tokyo 113-0034 Japan (e-mail: sekihara@ma.jst.go.jp).

S. Nagarajan is with the Keck Center for Integrative Neuroscience, University of California, San Francisco, CA 94143-0732 USA.

D. Poeppel is with the Department of Linguistics and Biology, University of Maryland, College Park, MD 20742 USA.

Y. Miyashita is with the Mind Articulation Project, Japan Science and Technology Corporation (JST), Tokyo 113-0034 Japan and is also with the Department of Physiology, The University of Tokyo, School of Medicine, Tokyo 113-0033 Japan.

Publisher Item Identifier S 0278-0062(99)02029-7.

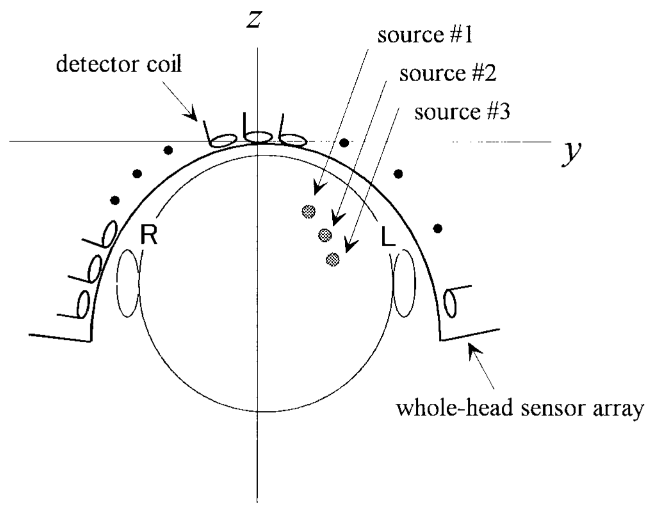

Fig. 1. Schematic view of the sensor-source configuration used in the computer simulation.

II. Method

Let us define the magnetic field measured by the mth detector coil at time t as $b_m(t)$ and a vector $\boldsymbol{b}(t) = (b_1(t), b_2(t), \ldots, b_M(t))^T$ as a set of measured data where M is the total number of detector coils. A total of P current-dipole sources is assumed to generate the biomagnetic field, and the locations of these sources are denoted as $(\boldsymbol{x}_1, \boldsymbol{x}_2, \ldots, \boldsymbol{x}_P)$. The magnitude of the pth dipole-source moment is defined as $s_p(t)$. The source magnitude vector is defined as $\boldsymbol{s}(t) = (s_1(t), s_2(t), \ldots, s_P(t))^T$. A spherical homogeneous conductor [4] is assumed and two tangential components, the ϕ and θ components, of the dipole-source moment are considered. The dipole orientation is defined as its normal vector $\boldsymbol{\eta}_p(t) = (\eta_p^\phi(t), \eta_p^\theta(t))^T$ where $\|\boldsymbol{\eta}_p(t)\| = 1$. We also define a $2P \times P$ matrix that expresses the orientations of all P dipole sources as $\boldsymbol{\Psi}(t)$ such that

$$\boldsymbol{\Psi}(t) = \begin{bmatrix} \boldsymbol{\eta}_1(t) & 0 & \cdots & 0 \\ 0 & \boldsymbol{\eta}_2(t) & \cdot & \vdots \\ \vdots & \cdot & \ddots & 0 \\ 0 & \cdots & 0 & \boldsymbol{\eta}_P(t) \end{bmatrix}. \tag{1}$$

The lead field vectors for the ϕ and θ components of the source at $\boldsymbol{x}$ are defined as $\boldsymbol{l}^\phi(\boldsymbol{x}) = (l_1^\phi(\boldsymbol{x}), l_2^\phi(\boldsymbol{x}), \ldots, l_M^\phi(\boldsymbol{x}))^T$ and $\boldsymbol{l}^\theta(\boldsymbol{x}) = (l_1^\theta(\boldsymbol{x}), l_2^\theta(\boldsymbol{x}), \ldots, l_M^\theta(\boldsymbol{x}))^T$. Here, $l_m^\phi(\boldsymbol{x})$ and $l_m^\theta(\boldsymbol{x})$ express the mth sensor output induced by the unit-magnitude source moment directed in the ϕ and θ directions, respectively. We define the lead field matrix for the source at $\boldsymbol{x}$ as $\boldsymbol{L}(\boldsymbol{x}) = [\boldsymbol{l}^\phi(\boldsymbol{x}), \boldsymbol{l}^\theta(\boldsymbol{x})]$, which represents the sensitivity of the sensor array at location $\boldsymbol{x}$. The composite lead field matrix for the entire set of P dipole sources is defined as $\boldsymbol{L}_c = [\boldsymbol{L}(\boldsymbol{x}_1), \boldsymbol{L}(\boldsymbol{x}_2), \ldots, \boldsymbol{L}(\boldsymbol{x}_P)]$. Then, the relationship between $\boldsymbol{b}(t)$ and $\boldsymbol{s}(t)$ is expressed as

$$\boldsymbol{b}(t) = [\boldsymbol{L}_c \boldsymbol{\Psi}(t)]\boldsymbol{s}(t) + \boldsymbol{n}(t) \tag{2}$$

where $\boldsymbol{n}(t)$ is the additive noise.

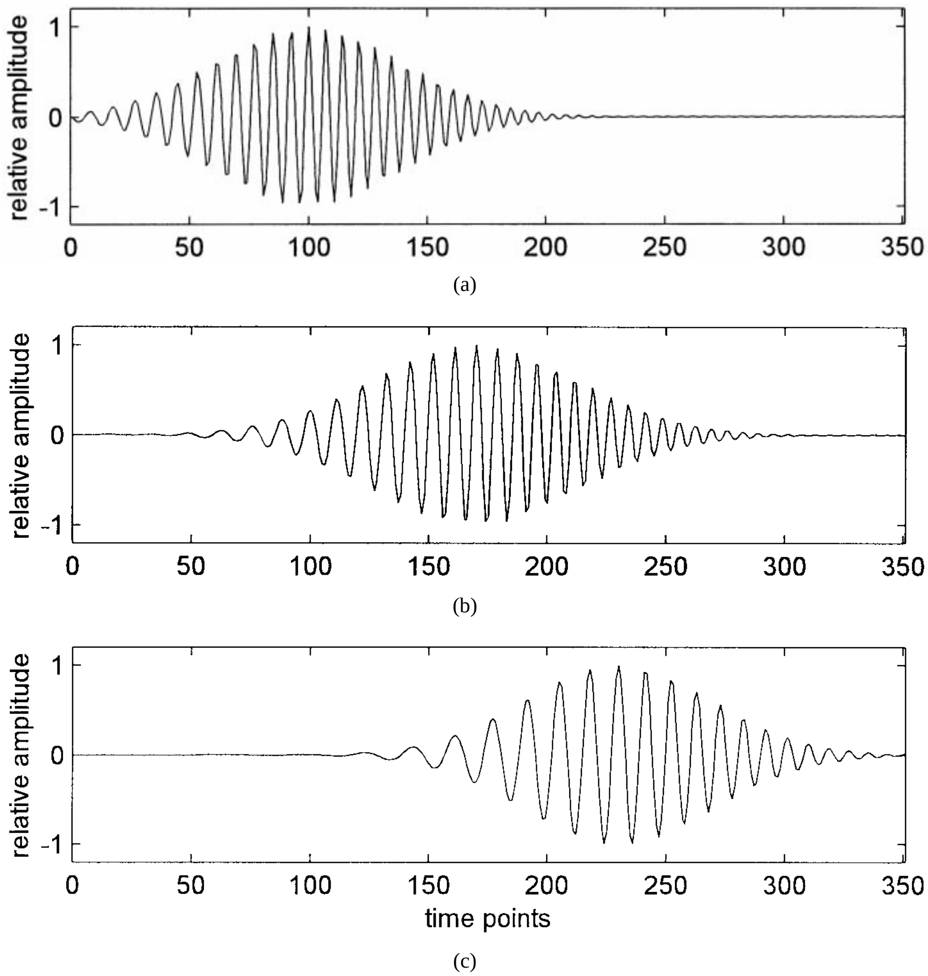

Fig. 2. Generated waveforms of ϕ components of: (a) first source; (b) second source; and (c) third source.

To formulate the time–frequency MUSIC algorithm, we assume that all dipole sources do not change their orientations during the time period of interest and we use time-independent $\boldsymbol{\Psi}$ to express the dipole source orientations. The time–frequency distribution matrices for $\boldsymbol{b}(t)$ and $\boldsymbol{s}(t)$ are defined as $\boldsymbol{C}_b(t,f)$ and $\boldsymbol{C}_s(t,f)$, which can be obtained by using any of the Cohen-class time–frequency distributions [2], [5], i.e.,

$$\boldsymbol{C}_b(t,f) = \iint_{-\infty}^{\infty} \Phi(\nu - t, \xi - f) \cdot \left[\int_{-\infty}^{\infty} \boldsymbol{b}(\nu + \tau/2)\boldsymbol{b}^T(\nu - \tau/2)e^{-2\pi i \xi \tau}\, d\tau\right] d\nu\, d\xi \tag{3}$$

and

$$\boldsymbol{C}_s(t,f) = \iint_{-\infty}^{\infty} \Phi(\nu - t, \xi - f) \cdot \left[\int_{-\infty}^{\infty} \boldsymbol{s}(\nu + \tau/2)\boldsymbol{s}^T(\nu - \tau/2)e^{-2\pi i \xi \tau}\, d\tau\right] d\nu\, d\xi. \tag{4}$$

Here, $\Phi(t,f)$ is the convolution kernel, which determines the characteristics of the resultant Cohen-class time–frequency distributions. The matrix $\boldsymbol{C}_b(t,f)$ is an $M \times M$ matrix. Its diagonal elements are the autotime–frequency distributions of the channel recordings and its off-diagonal elements are the crosstime–frequency distributions between different channel recordings. The matrix $\boldsymbol{C}_s(t,f)$ is a $P \times P$ matrix. Its diagonal elements are the autotime–frequency distributions of the source activities and its off-diagonal elements are the crosstime–frequency distributions between different source activities.

TABLE I
SOURCE PARAMETER VALUES ASSUMED FOR THE COMPUTER SIMULATION

source number	location (cm)	t_j	σ_j	b_j	a_j
j=1	(1.0, 4.0, −6.5)	230	100	0	4×10^{-4}
j=2	(1.0, 5.0, −8.0)	170	100	0.05	4×10^{-4}
j=3	(1.0, 5.5, −9.5)	100	100	0.1	4×10^{-4}

Using (2)–(4), we can derive

$$\boldsymbol{C}_b(t,f) = (\boldsymbol{L}_c\boldsymbol{\Psi})\boldsymbol{C}_s(t,f)(\boldsymbol{\Psi}^T\boldsymbol{L}_c^T) + \boldsymbol{C}_{sn}(t,f) + \boldsymbol{C}_{ns}(t,f) + \boldsymbol{C}_n(t,f) \tag{5}$$

where

$$\boldsymbol{C}_{sn}(t,f) = \iint_{-\infty}^{\infty} \Phi(\nu - t, \xi - f) \cdot \left[\int_{-\infty}^{\infty} (\boldsymbol{L}_c\boldsymbol{\Psi})\boldsymbol{s}(\mu + \tau/2) \cdot \boldsymbol{n}^T(\nu - \tau/2)e^{-2\pi i \xi \tau}\, d\tau\right] d\nu\, d\xi \tag{6}$$

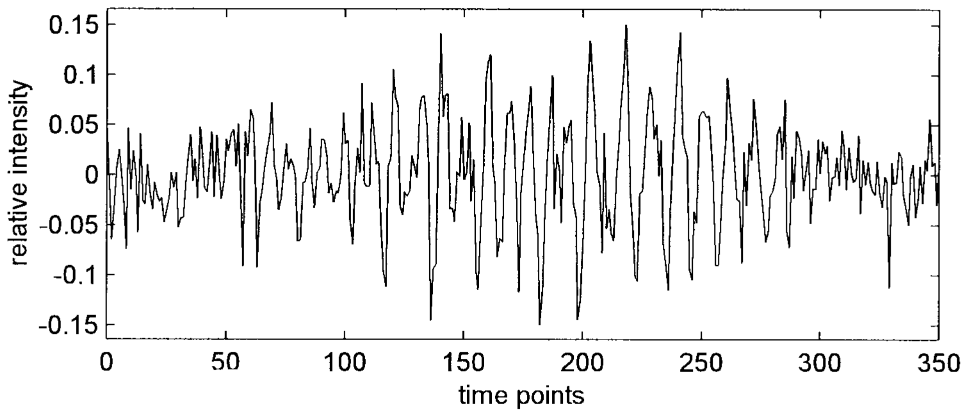

(a)

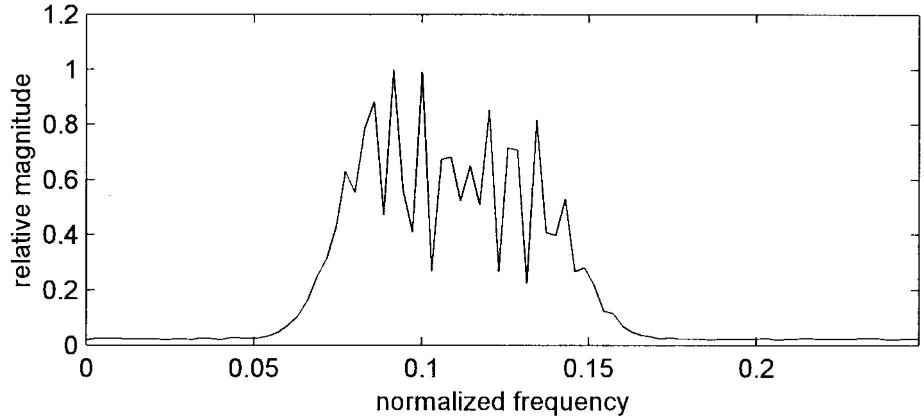

(b)

Fig. 3. (a) Waveform of the generated magnetic field from one representative channel located above the left hemisphere. (b) Power spectrum of the generated magnetic field obtained by averaging the spectra from all channels.

$$\boldsymbol{C}_{ns}(t,f) = \iint_{-\infty}^{\infty} \Phi(\nu - t, \xi - f) \cdot \left[\int_{-\infty}^{\infty} \boldsymbol{n}(\nu + \tau/2) \cdot \boldsymbol{s}^T(\nu - \tau/2)(\boldsymbol{\Psi}^T \boldsymbol{L}_c^T) e^{-2\pi i \xi \tau}\, d\tau\right] d\nu\, d\xi \quad (7)$$

and

$$\boldsymbol{C}_{n}(t,f) = \iint_{-\infty}^{\infty} \Phi(\nu - t, \xi - f) \cdot \left[\int_{-\infty}^{\infty} \boldsymbol{n}(\nu + \tau/2)\boldsymbol{n}^T(\nu - \tau/2) e^{2\pi i \xi \tau}\, d\tau\right] d\nu\, d\xi. \quad (8)$$

Let us define the region of interest in the time–frequency domain as Ω. This region contains the signal of interest and we localize sources by using time–frequency components in this region. The matrices $\boldsymbol{\Upsilon}_b$ and $\boldsymbol{\Upsilon}_s$ are obtained by averaging $\boldsymbol{C}_b(t,f)$ and $\boldsymbol{C}_s(t,f)$ over this target time–frequency region Ω, i.e.,

$$\boldsymbol{\Upsilon}_b = \iint_{\Omega} \boldsymbol{C}_b(t,f)\, dt\, df \quad \text{and} \quad \boldsymbol{\Upsilon}_s = \iint_{\Omega} \boldsymbol{C}_s(t,f)\, dt\, df \quad (9)$$

where $\int\int_{\Omega}$ indicates the integral over this target time–frequency region. We denote the number of sources whose activities have time–frequency components in the target region as P_{Ω}. Note that the matrix $\boldsymbol{\Upsilon}_s$ is a $P_{\Omega} \times P_{\Omega}$ matrix.

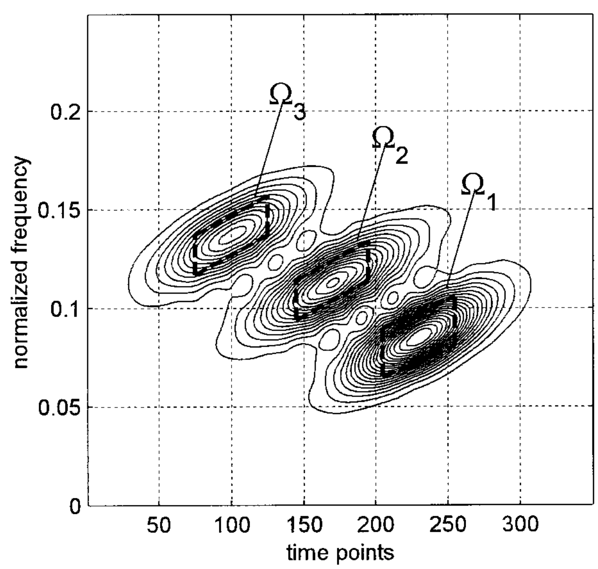

Fig. 4. Smoothed pseudo-Wigner–Ville time–frequency distribution of computer generated neuromagnetic data. The time–frequency maps were calculated from all channel recordings, and the results obtained by averaging all these maps are shown. The frequency is normalized such that the Nyquist frequency is equal to 0.5. The three quadrangular areas denoted by Ω_1, Ω_2, and Ω_3 are the target regions used for the source-estimation experiments.

We assume that the noise and signal are uncorrelated in the target region. This assumption leads to $\int\int_{\Omega} \boldsymbol{C}_{ns}(t,f)\ dt\ df = \int\int_{\Omega} \boldsymbol{C}_{sn}(t,f)\ dt\ df = 0$. We also assume that the noise is white

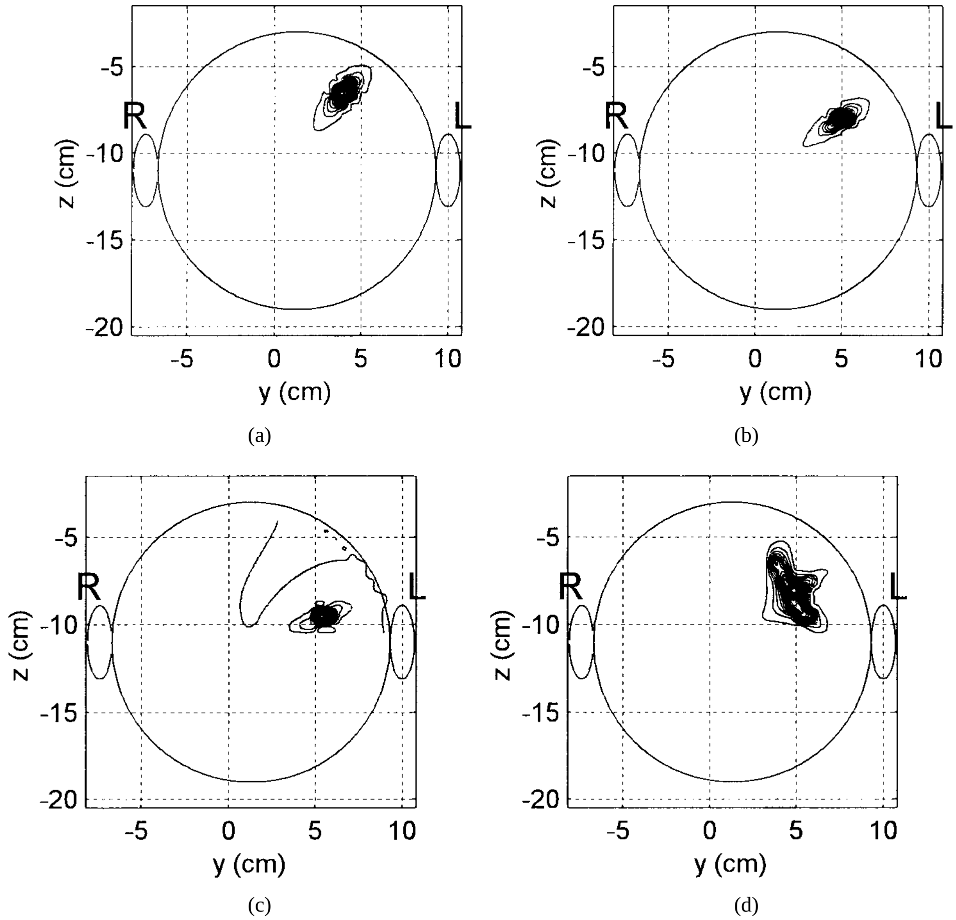

Fig. 5. MUSIC-localizing function on the plane $x = 1$ cm. The time–frequency MUSIC algorithm [(13)] was used with the target region set at (a) Ω_1, (b) Ω_2, and (c) Ω_3. (d) The conventional MUSIC algorithm [(17)] was used.

Gaussian, so the expected value of $\boldsymbol{C}_n(t,f), \langle \boldsymbol{C}_n(t,f)\rangle$ is equal to $\sigma_D^2 \boldsymbol{I}$ where $\langle\cdot\rangle$ indicates the ensemble average and σ_D^2 is the noise power density. Accordingly, if the target region is sufficiently large, replacing the ensemble average by the integration over the target region we have $\int\int_\Omega \boldsymbol{C}_n(t,f)\, dt\, df = \sigma^2 \boldsymbol{I}$ where σ^2 is the total noise power in the target region. Therefore, we finally derive the relationship

$$\boldsymbol{\Upsilon}_b = (\boldsymbol{L}_c\boldsymbol{\Psi})\boldsymbol{\Upsilon}_s(\boldsymbol{\Psi}^T\boldsymbol{L}_c^T) + \sigma^2\boldsymbol{I}. \tag{10}$$

Denoting the noise-level eigenvectors of $\boldsymbol{\Upsilon}_b$ as $\boldsymbol{u}_j$, where $j = P_\Omega + 1, \ldots, M$, (10) becomes

$$(\boldsymbol{\Upsilon}_b - \sigma^2\boldsymbol{I})\boldsymbol{u}_j = (\boldsymbol{L}_c\boldsymbol{\Psi})\boldsymbol{\Upsilon}_s(\boldsymbol{\Psi}^T\boldsymbol{L}_c^T)\boldsymbol{u}_j = 0,$$
$$j = P_\Omega + 1, \ldots, M. \tag{11}$$

The matrix $\boldsymbol{L}_c$ is a full-column-rank matrix. Thus, when the matrix $\boldsymbol{\Upsilon}_s$ is a full-rank matrix, we get

$$(\boldsymbol{\Psi}^T\boldsymbol{L}_c^T)\boldsymbol{u}_j = 0, \qquad \text{for } j = P_\Omega + 1, \ldots, M. \tag{12}$$

The above equation indicates that source locations can be obtained by checking the orthogonality between the sensor lead field with an optimum orientation $\boldsymbol{L}(\boldsymbol{x})\boldsymbol{\eta}_{\text{opt}}$ where $\boldsymbol{\eta}_{\text{opt}}$ represents the normal vector in the optimum orientation, and the noise-level eigenvectors $\boldsymbol{u}_j$ $(j = P_\Omega + 1, \ldots, M)$.

This orthogonality can be evaluated by calculating the following function:

$$J(\boldsymbol{x}) = 1/\lambda_{\min}(\boldsymbol{L}^T(\boldsymbol{x})\boldsymbol{Z}_N\boldsymbol{Z}_N^T\boldsymbol{L}(\boldsymbol{x}), \boldsymbol{L}^T(\boldsymbol{x})\boldsymbol{L}(\boldsymbol{x})) \tag{13}$$

where $\lambda_{\min}(\cdot,\cdot)$ indicates the minimum generalized eigenvalue of the matrix pair in parenthesis and the matrix $\boldsymbol{Z}_N$ is defined as $\boldsymbol{Z}_N = [\boldsymbol{u}_{P_\Omega+1}, \ldots, \boldsymbol{u}_M]$. This $J(\boldsymbol{x})$, referred to as the localizing function, is calculated point-by-point in a volume where sources can exist. Each location where $J(\boldsymbol{x})$ forms a peak is chosen as the location of one dipole source.

Equation (13) was obtained under the assumption that dipole sources do not change their orientations during the time period of interest. It is worth noting that when this assumption does not hold and the source orientations change, this localizing function can still be used to detect source locations. In such cases, instead of (10) we have the relationship

$$\boldsymbol{\Upsilon}_b = \boldsymbol{L}_c\tilde{\boldsymbol{\Upsilon}}_s\boldsymbol{L}_c^T + \sigma^2\boldsymbol{I} \tag{14}$$

where $\tilde{\boldsymbol{\Upsilon}}_s = \int\int_\Omega \tilde{\boldsymbol{C}}_s(t,f)\, dt\, df$, and $\tilde{\boldsymbol{C}}_s(t,f)$ is obtained from

$$\tilde{\boldsymbol{C}}_s(t,f) = \iint_{-\infty}^{\infty} \Phi(\nu - t, \xi - f) \cdot \left[\int_{-\infty}^{\infty} \boldsymbol{\Psi}(\nu + \tau/2)\boldsymbol{s}(\nu+\tau/2) \cdot \boldsymbol{s}^T(\nu - \tau/2)\boldsymbol{\Psi}^T(\nu - \tau/2)e^{-2\pi i\xi\tau}\, d\tau\right] d\nu\, d\xi. \tag{15}$$

Therefore, assuming that the matrix $\tilde{\boldsymbol{\Upsilon}}_s$ is a full-rank matrix, we also obtain the relationship

$$\boldsymbol{L}_c^T\boldsymbol{u}_j = 0, \qquad \text{for } j = P_\Omega + 1, \ldots, M. \tag{16}$$

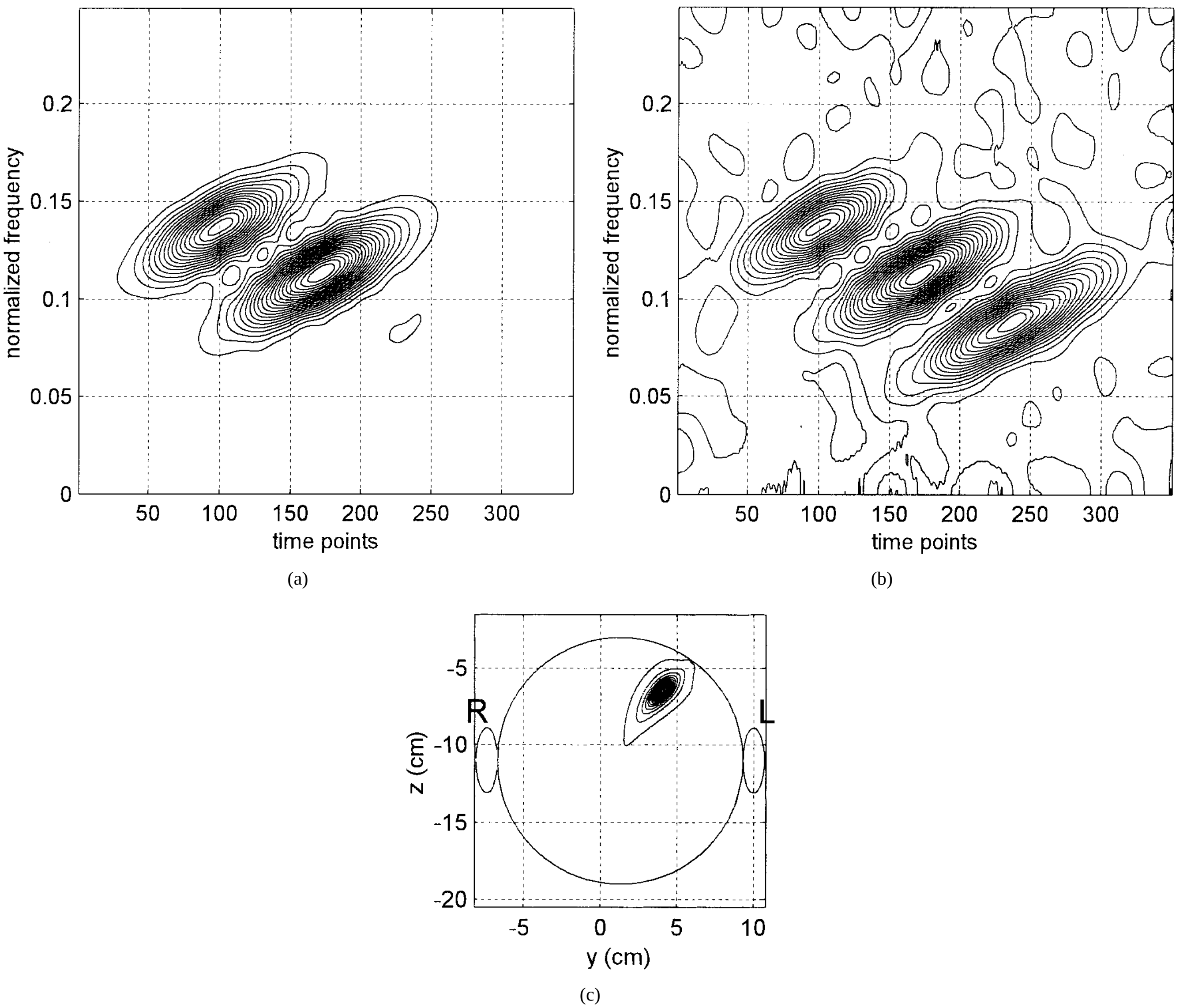

Fig. 6. Smoothed pseudo-Wigner–Ville time–frequency distribution of the neuromagnetic data used for the time jitter experiments. The time–frequency maps were calculated from all channel recordings, and the results obtained by averaging all these maps are shown. (a) Time–frequency map obtained from the waveform averaged across all epochs. (b) Time–frequency map obtained by averaging maps from all raw epochs. (c) Time–frequency MUSIC localizing function on the plane $x = 1$ cm. The target region was set at Ω_1 shown in Fig. 4 and the matrix $\boldsymbol{\Upsilon}_b$ was calculated using $\boldsymbol{\Upsilon}_b = \langle \int\int_\Omega \boldsymbol{C}_b(t, f)\, dt\, df \rangle_{\text{epoch}}$.

Since the source locations that satisfy (16) also satisfy (12), the localizing function in (13) is effective even when the source orientations are not time independent and change during the period of interest.

It is informative to compare (13) with the localizing function used in the conventional time-domain MUSIC algorithm. This conventional localizing function is expressed as [3]

$$J(\boldsymbol{x}) = 1/\lambda_{\min}(\boldsymbol{L}^T(\boldsymbol{x})\boldsymbol{E}_N\boldsymbol{E}_N^T\boldsymbol{L}(\boldsymbol{x}), \boldsymbol{L}^T(\boldsymbol{x})\boldsymbol{L}(\boldsymbol{x})) \qquad (17)$$

where $\boldsymbol{E}_N = [\boldsymbol{e}_{P+1}, \ldots, \boldsymbol{e}_M]$ and $\boldsymbol{e}_j$ $(j = P+1, \ldots, M)$ indicates the noise-level eigenvectors of the measured-data covariance matrix. This measured-data covariance matrix is obtained by averaging $\boldsymbol{b}(t)\boldsymbol{b}^T(t)$ during the time period of interest. The only difference between the proposed and the conventional MUSIC algorithms is that the proposed algorithm uses $\boldsymbol{Z}_N$ instead of $\boldsymbol{E}_N$ in the conventional algorithm.

III. Computer Simulation

We performed a computer simulation to test the validity of the proposed method. We used the coil configuration of a 148-channel whole-head Magnes 2500WH$^{\text{TM}}$ biomagnetic measurement system (Biomagnetic Technologies Inc., San Diego, CA). The coordinate origin was defined at the center of the coil array. The z direction was defined as the direction perpendicular to the plane of the detector coil located at this center. The x direction was defined as that from the posterior to the anterior, and the y direction was defined as that from the left to the right hemisphere.

Three signal dipole sources were assumed to exist on the same plane ($x = 1.0$ cm). The configuration of this computer simulation is shown schematically in Fig. 1. The simulated magnetic field was calculated at 351 time points. To generate the simulated neuromagnetic field, the ϕ components of the three sources $w_\phi^j(t), (j = 1, 2, 3)$ were all Gaussian amplitude modulated and frequency modulated, i.e., $w_\phi^j(t) = \exp[-(t - t_j)^2/(2\sigma_j^2)] \cos[2\pi(a_j t + b_j)(t - t_j)]$. The θ components of the three sources were set to zero. The values for t_j, σ_j, a_j, b_j and the assumed source locations are listed in Table I, and the generated waveforms for the ϕ components of the three sources are shown in Fig. 2.

Uncorrelated Gaussian noise was added to make the final signal-to-noise ratio (SNR) equal to two. The SNR was defined as the ratio of the Frobenius norm of the signal-magnetic-field data matrix to that of the noise matrix. The waveform of the generated magnetic field from one representative channel located above the left hemisphere is shown in Fig. 3(a) and the power spectrum obtained by averaging the spectra from all channels is shown in Fig. 3(b). These figures indicate that the signals from the three sources cannot be separated in either the time domain or in the frequency domain.

The smoothed pseudo-Wigner–Ville transform was calculated in order to obtain the time–frequency distribution of the computer generated data. The convolution kernel in (3) and (4) was chosen such that it was equal to a multiplication of a function of t and that of f each derived by Fourier transforming the hamming window with a window size of 39 data points. The time–frequency maps were calculated from all channel recordings, and the results obtained by averaging all these maps are shown in Fig. 4. Three time–frequency components are clearly resolved.

The time–frequency MUSIC algorithm was then applied by setting the target time–frequency region as the regions indicated by Ω_1, Ω_2, and Ω_3 in Fig. 4. The results are shown in Fig. 5. The contours in Fig. 5(a)–(c) show the relative value of the MUSIC localizing function in (13) on the plane $x = 1$ cm and each area where the localizing function reaches a peak is considered to be the location of one dipole source. The (y, z) coordinates of the peak locations in Fig. 5(a), (b), and (c) are (3.9, -6.5), (4.8, -8.1), and (5.4, -9.5), respectively. Comparison with the original source locations listed in Table I shows that the time–frequency MUSIC algorithm accurately localized the three sources, and these results verify the validity of the proposed algorithm. The conventional MUSIC algorithm [3] was applied to the same computer-generated data [Fig. 5(d)], but the conventional localizing function in (17) was not able to resolve the three sources. The results in Fig. 5 demonstrate the effectiveness of the proposed method.

It is sometimes possible that a transient event-related signal is not time locked to the stimulus and has a time jitter among multiple-epoch recordings [6]. We next show that a minor modification of the proposed algorithm allows source locations to be estimated from such a nontime-locked event-related signal. The simulated magnetic field data was calculated assuming that the first source has a time jitter t_z, i.e., its ϕ component has a form $w_\phi^1(t - t_z)$. Here, t_z was generated by using a uniform random number ranging from -50 to 50 time points, and a total of 64 raw-epoch data was generated. The SNR of each raw-epoch data was set at 0.25. Two kinds of time–frequency maps were obtained; one was obtained by using the simulated magnetic-field waveforms averaged across all raw epochs and the other was obtained by averaging time–frequency maps across all raw epochs. The results are shown in Fig. 6.

In the time–frequency distribution in Fig. 6(a), the time–frequency component generated from the first source has almost disappeared because of the time jitter. Conversely, this component is clearly observable (although it is significantly blurred compared to that in Fig. 4) in the time–frequency distribution in Fig. 6(b), which is obtained by averaging a time–frequency map from each set of raw-epoch data. This observation suggests that if we calculate the matrix $\boldsymbol{\Upsilon}_b$ such that $\boldsymbol{\Upsilon}_b = \langle \int\int_\Omega \;\; \boldsymbol{C}_b(t, f) \;\; dt \;\; df \rangle_{\text{epoch}}$ where $\langle \cdot \rangle_{\text{epoch}}$ indicates the average over epochs we can localize sources for nontime-locked activities. The localization function in (13) was calculated with $\boldsymbol{\Upsilon}_b$ obtained in the above-mentioned manner and with the same target region Ω_1 shown in Fig. 4. The results are shown in Fig. 6(c). Here, the first source is clearly detected. The (x, y) coordinates of the peak in this figure are (4.1, -6.5), which are very close to the assumed location of the first source. The results obtained here show that the proposed algorithm is, in principle, effective for localizing an evoked source whose activation is not time-locked to the stimulus.

IV. Discussion

Although the quadratic Cohen-class distributions can provide high-resolution time–frequency maps, they are known to contain significant amount of spurious crossterms when the distribution contains multiple components. The convolution kernel $\Phi(t, f)$ in (3) or (4) should therefore be chosen so as to reduce the amount of such spurious cross terms at the minimum sacrifice of the resolution. As a result, the kernel determines the tradeoff between the resolution and the amount of such spurious crossterms. The relationship between several specific choices of the kernel and the properties of the resultant time–frequency distributions has been well studied in the field of time–frequency analysis. A detailed discussion on the choices of the kernel and properties of the resultant time–frequency distributions are found in [2] and [5].

In our computer simulation, we used the smoothed pseudo-Wigner–Ville representation, which uses the kernel separable in terms of time and frequency. This choice, however, is somewhat arbitrary and any other Cohen-class representation can be used for our computer generated data. For actual spontaneous or event-related MEG, the choice of the kernel must be made by taking several properties of the MEG data to be analyzed into consideration. Such properties include the number of time–frequency components, how close they are, and how localized or diffused they are. The optimum kernel for analyzing various types of transient MEG data needs to be investigated.

The proposed algorithm is suited to localizing sources for transient and nonstationary MEG signals. There are several situations in MEG measurements in which a transient signal is observed but its origin is not adequately established. A well-known example of such signals is visual or auditory gamma-band activity, which may have a relationship with feature binding in a cognitive process or even with consciousness [6], [7]. Other examples of such signals include human-spontaneous MEG [8]. We plan to apply the proposed algorithm to such nonstationary signals and we will report these results in the near future.

References

[1] M. Hämäläinen, R. Hari, R. J. IImoniemi, J. Knuutila, and O. V. Lounasmaa, "Magnetoencephalography-theory, instrumentation, and applications to noninvasive studies of the working human brain," *Rev. Mod. Phys.*, vol. 65, pp. 413–497, 1993.

[2] L. Cohen, *Time–Frequency Analysis: Theory and Applications*. Englewood Cliffs, NJ: Prentice-Hall, Inc., 1994.

[3] J. C. Mosher, P. S. Lewis, and R. M. Leahy, "Multiple dipole modeling and localization from spatio-temporal MEG data," *IEEE Trans. Biomed. Eng.*, vol. 39, pp. 541–557, 1992.

[4] J. Sarvas, "Basic mathematical and electromagnetic concepts of the biomagnetic inverse problem," *Phys. Med. Biol.*, vol. 32, pp. 11–22, 1987.

[5] F. Hlawatsch and G. F. Boudreaux-bartels, "Linear and quadratic time–frequency signal representations," *IEEE Signal Processing Mag.*, vol. 9, pp. 21–67, Apr. 1992.

[6] C. Tallon-Baudry, O. Bertrand, C. Delpuech, and J. Pernier, "Oscillatory γ-band (30–70 Hz) activity induced by a visual search task in humans," *J. Neurosci.*, vol. 17, pp. 722–733, 1997.

[7] R. Llinas and U. Ribary, "Coherent 40-Hz oscillation characterizes dream state in humans," *Proc. Nat. Acad. Sci.*, vol. 90, pp. 2078–2081, 1993.

[8] R. Hari and R. Salmelin, "Human cortical oscillations: a neuromagnetic view through the skull," *Trends Neurosci.*, vol. 20, pp. 44–49, 1997.